

A thin film lithium niobate near-infrared platform for multiplexing quantum nodes

Received: 15 April 2024

Accepted: 12 November 2024

Published online: 02 December 2024



Daniel Assumpcao^{1,4}✉, Dylan Renaud^{1,4}✉, Aida Baradari¹, Beibei Zeng², Chawina De-Eknamkul², C. J. Xin¹, Amirhassan Shams-Ansari³, David Barton¹, Bartholomeus Machielse² & Marko Loncar¹✉

Practical quantum networks will require multi-qubit quantum nodes. This in turn will increase the complexity of the photonic circuits needed to control each qubit and require strategies to multiplex memories. Integrated photonics operating at visible to near-infrared (VNIR) wavelength range can provide solutions to these needs. In this work, we realize a VNIR thin-film lithium niobate (TFLN) integrated photonics platform with the key components to meet these requirements, including low-loss couplers (<1 dB/facet), switches (>20 dB extinction), and high-bandwidth electro-optic modulators (>50 GHz). With these devices, we demonstrate high-efficiency and CW-compatible frequency shifting (>50% efficiency at 15 GHz), as well as simultaneous laser amplitude and frequency control. Finally, we highlight an architecture for multiplexing quantum memories and outline how this platform can enable a 2-order of magnitude improvement in entanglement rates over single memory nodes. Our results demonstrate that TFLN can meet the necessary performance and scalability benchmarks to enable large-scale quantum nodes.

The distribution of quantum entanglement across continental distances via quantum networks is an enabling technology for a variety of applications, including quantum key distribution, sensing, and distributed quantum computing^{1,2}. An important step towards this goal is generation of remote entanglement between spatially separated quantum memory nodes. Despite great experimental progress^{3–8}, the rate of entanglement generation across km scale distances has been limited to the sub-Hz regime. Transitioning these experiments from proof-of-concept demonstrations to practical networking technology requires increasing the number of qubits to 100s–1000s or even beyond. This would enable both increasing entanglement generation rates through multiplexing as well as the utilization of qubits as auxiliary memories for multi-qubit protocols such as entanglement distillation or entanglement swapping^{2,9,10}.

To effectively scale the number of qubits per node, however, several key technical innovations are necessary. First, the qubits and associated controls must be manufacturable in a scalable way. While

solid-state qubits satisfy this criteria, their optical control currently requires bulky off-the-shelf lasers as well as acousto-optic and electro-optic modulators. Moreover, solid-state qubits, such as color centers, suffer from variations in their transition frequency which prevents entanglement generation between these qubits¹¹. Therefore, a method to efficiently frequency shift photons emitted by the qubits is required to overcome this inhomogeneous broadening. Finally, the ability to connect any of the on-chip memories to a common optical channel (e.g., optical fiber) is essential to enable temporal multiplexing that can significantly increase the entanglement generation rate. This can be accomplished using a large on-chip switch network. All of these functionalities must be implemented with minimal additional insertion loss. This can be challenging since, the majority of quantum emitters have optical transitions in the visible and near-infrared regime (400 nm–1000 nm)^{12–17}, which is above the bandgap of traditional photonic integrated circuit (PIC) platforms such as indium phosphide or silicon¹⁸. On the other hand, silicon nitride does offer a suitable

¹John A. Paulson School of Engineering and Applied Sciences, Harvard University, Cambridge, MA, USA. ²AWS Center for Quantum Networking, Boston, MA, USA. ³DRS Daylight Solutions, San Diego, CA, USA. ⁴These authors contributed equally: Daniel Assumpcao, Dylan Renaud.

✉ e-mail: dassumpcao@g.harvard.edu; renaud@g.harvard.edu; loncar@g.harvard.edu

transparency window, but available modulation approaches based on the thermo-optic effect or the piezo-electric effect, are slow and cannot achieve 10s to 100s MHz switching speeds required for multiplexing^{19–21}.

Recently thin-film lithium-niobate (TFLN) on insulator has emerged as a promising PIC platform due to its combination of large electro-optic (EO) coefficient, low optical losses, and large transparency window extending to 400 nm^{22,23}. High-performance visible systems have been fabricated on TFLN including low-loss passive devices and active modulators^{16,24–27}.

In this work, we extend these results and demonstrate the key building blocks needed to scale quantum networking technology. We propose a TFLN photonic-enabled architecture to realize a scalable quantum node and demonstrate the necessary devices to realize this vision. This includes high-efficiency couplers with coupling efficiencies below 1 dB/facet, high-bandwidth phase modulators which we utilize to frequency shift a CW tone by up to 15 GHz with efficiencies beyond 50%, and optical switches with high extinction ratio (20 dB) and suitable EO bandwidth for multiplexing. To both highlight the scalability of the platform and provide a compact solution for qubit optical control hardware, we also demonstrate a multi-component laser control unit PIC, which can be used to provide amplitude and frequency control of an input laser in our proposed architecture.

Results

Our proposed TFLN architecture to realize a scalable quantum network node is depicted in Fig. 1. It consists of a combination of amplitude modulators (AM), frequency shifting via phase modulators (PM), switches, and high-efficiency fiber couplers all interfaced with a large array of quantum memory (QM) devices (see supplementary information section 2 for detailed discussion). These devices provide the necessary functionalities to effectively scale the optical control and multiplex the output of the QM modules. We note that although in our schematic the QMs are depicted as integrated within the PIC, this is not a requisite for our architecture. For example, the TFLN control PIC can

be connected to QMs on a separate chip using low-loss fiber couplers^{22,28}, that we discuss next.

For high-fidelity and high-rate entanglement generation and distribution, minimizing insertion loss of all optical components, including the on/off-chip coupling losses, is paramount. Inspired by the ultra-low coupling efficiencies achieved using adiabatic tapered fiber-to-chip interfaces in diamond and silicon-nitride platforms, we developed an adiabatic fiber coupler in TFLN (Fig. 2)^{18,28–30}. The primary challenge for low-loss adiabatic fiber couplers in TFLN is underlying oxide cladding that can support leaky modes. Therefore, to achieve efficient coupling between the TFLN and optical fiber, the TFLN waveguide must be suspended. We implement our design by first using a TFLN bilayer taper³¹ to adiabatically convert the rib waveguide mode to a ridge waveguide. Next, the ridge width is decreased to create an inverted taper (“lower taper”) which expands the mode (Fig. 2a) so that it can be coupled to a tapered optical fiber. A clamp is included at the end of the suspended lower taper to prevent collapsing of the device. A tapered optical fiber touches down on the TFLN lower taper, ensuring an efficient, adiabatic mode transfer between the fiber and TFLN waveguides. The geometry was optimized via finite-difference-time-domain (FDTD) simulations, with a peak simulated efficiency of ~99% (Fig. 2a inset). The achievable efficiency in simulations is primarily limited by the lower tip dimension, which in our fabricated devices is ~60 nm. Fabricated devices (for details, see “Methods”) were characterized and featured coupling losses as low as 0.9 dB/facet (81.2% efficiency), with optical bandwidths exceeding 100 nm. The discrepancy between simulated and measured losses is attributed to scattering at the bilayer taper rib-ridge mode conversion interface, shown in the inset of Fig. 2a. Still, we emphasize that measured fiber coupling values are state-of-the-art for TFLN couplers at visible to near-infrared wavelengths, and are comparable to the best demonstrated at telecom wavelengths as well^{32,33}.

Spatial switches are required to route photons for both multiplexing and on-chip entanglement generation. We implement an EO switch using a Mach-Zehnder modulator (MZM) based design with

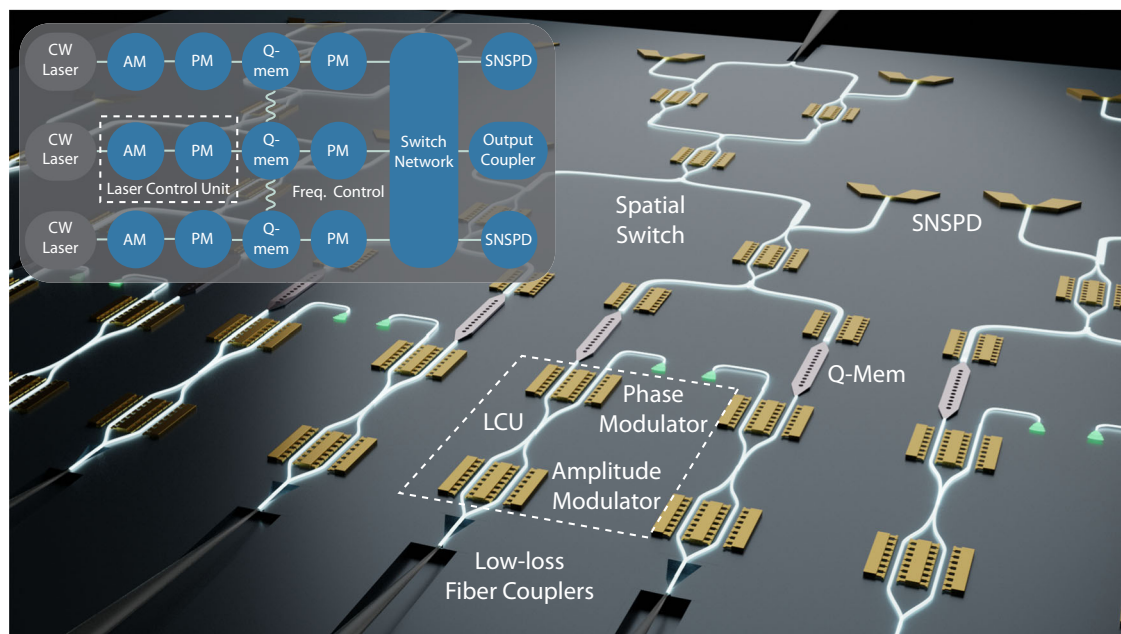


Fig. 1 | Illustration of proposed TFLN-enabled quantum node. Light from a laser is fiber-coupled to TFLN PIC and then passes through a laser control unit (LCU) that consists of an amplitude modulator (AM) followed by a phase modulator (PM). The LCU provides amplitude and frequency control of the input CW laser, needed to address a quantum memory module (Q-Mem). We emphasize that while the Q-Mem is shown on chip for illustrative purposes, it can be effectively linked to the main

control PIC via optical fiber and low-loss couplers demonstrated in this work. Another PM enables frequency control of single photons entangled with the Q-Mem. Finally, a switch network is used to multiplex the various memories together. Photons passed through the switch are routed to either on-chip single photon detectors (SNSPDs) or to a low-loss output fiber coupler to route photons to the off-chip fiber network.

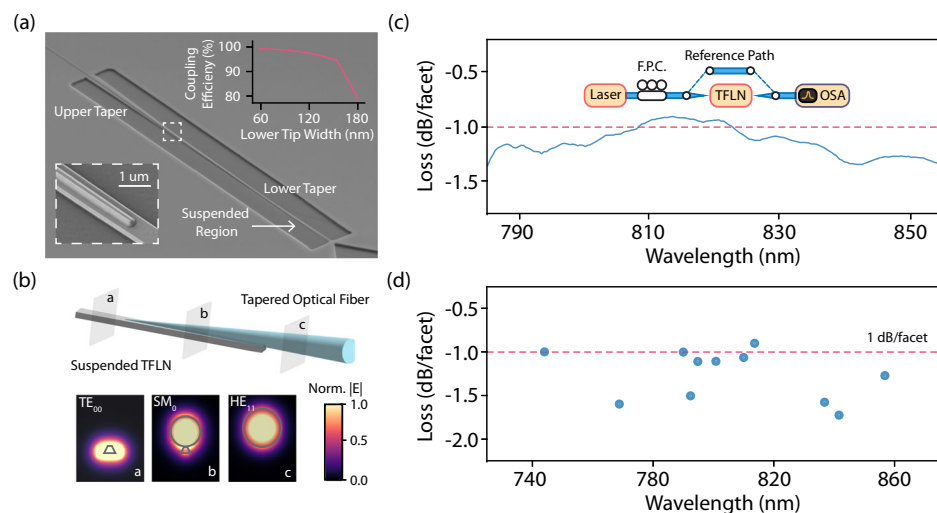


Fig. 2 | High-efficiency tapered optical fiber coupler for VNIR TFLN. **a** Scanning electron micrograph (SEM) of a free-standing bilayer adiabatic fiber coupler realized in TFLN. Light from a tapered optical fiber is adiabatically transferred to a ridge waveguide mode of a TFLN “lower taper”, and then using “upper taper” is transferred into the rib-waveguide mode. (lower inset) SEM magnifying the bilayer transition region. (upper inset) Simulated coupling efficiency as a function of lower taper tip width, with a maximum simulated efficiency of ~99%. **b** Schematic of the

TFLN-fiber interface alongside optical mode simulations at various cross-sections. The simulations illustrate the transition from TFLN waveguide mode to optical fiber mode. **c** Coupling loss measurements, showing a minimum chip-to-fiber coupling loss of 0.9 dB/facet at ~810 nm. **d** Minimum coupling loss and corresponding minimum loss wavelengths measured across a variety of devices, demonstrating reproducible coupling losses below 1.5 dB/facet.

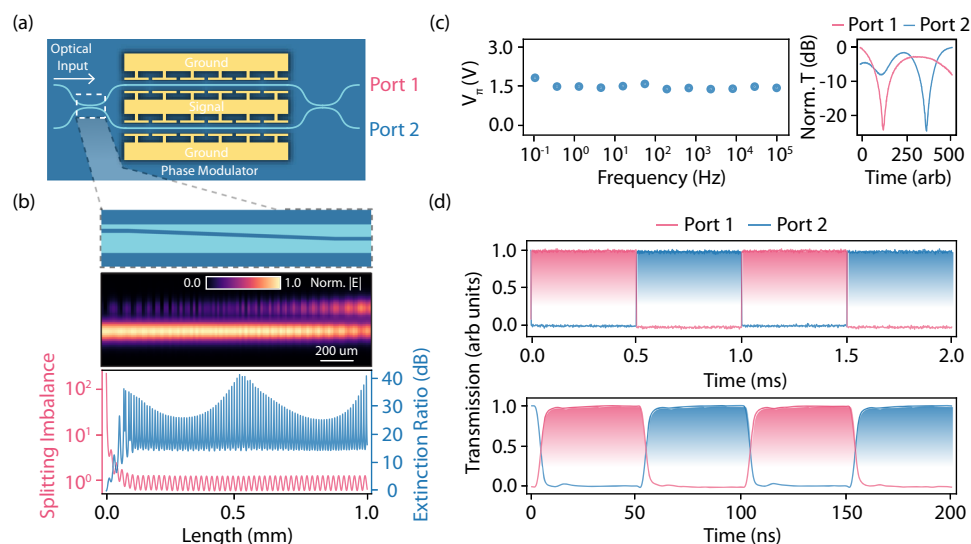


Fig. 3 | TFLN switches. **a** Diagram of a TFLN Mach-Zehnder modulator (MZM) based optical switch. **b** (top) Diagram and EME simulation of the adiabatic 2 × 2 coupler used in the switch. (bottom) Simulated coupler splitting ratio and corresponding modulator extinction ratio as a function of length. For lengths longer than the adiabaticity criterion (>100 μm), we observe a reduced dependence of split

ratio and extinction on device length, as expected. **c** Experimentally measured 5 mm long MZI switch features (left) a flat V_{π} of 1.5 V and (right) extinction ratio >20 dB for both ports. **d** Switching demonstration of the device, showing stable switching at both kHz and MHz time scales.

2 × 2 couplers at the input and output of the device (Fig. 3a). Adiabatic couplers are used for the 2 × 2 splitter to ensure fabrication robustness (Fig. 3b) (see “Methods” for additional design details)^{34,35}. We use numerical simulations to evaluate the splitting imbalance of the coupler, defined as the ratio of powers at the two output ports when coupler is excited using a single input port. We also evaluate the maximum extinction ratio achievable by a Mach Zehnder modulator utilizing two of these couplers due to the simulated splitting imbalance (Fig. 3b). Although the splitting ratio and corresponding modulator extinction ratio still depends on the length of the coupler,

likely due to partial coupling of the two waveguides on the imbalanced width side of the splitter, splitting imbalances are still close to 1 and extinction ratio of 15 dB can still be achieved even in the worst case. This indicates tolerance to fabrication imperfections. Fabricated devices feature an on-chip loss of 0.4 dB per switch, which is limited by on-chip propagation losses (see methods for details). To control the switch, we employ capacitive lumped element electrodes (as opposed to traveling-wave designs discussed below) to limit power consumption. A half-wave voltage (V_{π}) of ~1.5 V is measured for a 5 mm modulator, with extinction ratios greater than 20 dB on

both ports (Fig. 3c). We note that low-frequency roll off of the electro-optic response of a modulator can result in observed operational bias drifts in TFLN devices³⁶. In our work, the observed V_{π} is flat as a function of frequency down to 0.1 Hz which is important both for low-frequency switching operation and achieving a stable modulator bias³⁶. This excellent low-frequency response is due to engineering of the TFLN-electrode interface and process conditions and is sufficient to enable simple electrical biasing of the modulator with minimal electrical feedback (see supplementary information section 2 for additional details). We leverage this flat response to demonstrate switching between the two ports at kHz and MHz timescales, both of which are relevant for memory and photon operations, respectively, for typical solid-state emitters (Fig. 3d)^{4,13,37,38}. Importantly, these capacitive electrodes do not dissipate significant power in the hold state, and only ~100 W for 10 MHz switching, (see supplementary information section 2 for details). This suggests that large switch networks can be created with minimal electrical overhead, making them suitable for multiplexing quantum memories even at cryogenic temperatures.

To overcome the inhomogeneous distribution of QM optical transitions, our platform incorporates optical frequency-shifting capabilities. We choose to utilize a serrodyne-based frequency approach whereby a linear advance in phase is emulated using a sawtooth wave with an amplitude of 2π applied to the phase modulator. This approach in principle can enable frequency shifts with unity efficiency and functions irrespective of the temporal shape of the input light (Fig. 4a)^{39–44} (see supplementary information section 1 for details). The latter is especially important, as quantum memories can possess narrow transitions with correspondingly long photon lifetimes (ns or longer). Beyond this, the frequency precision of serrodyning is ultimately set by the temporal jitter and the phase noise of the electrical wave, applied to the modulator, which can be very high for state-of-the-art electronics. For example, we estimate that the digital to analog converter (DAC) used in our work (Keysight M8196A) results in jitter equivalent to a 17 Hz linewidth, which is significantly smaller than the MHz linewidths of the solid-state qubits considered in this work (see supplementary section 1 for details). The challenge with serrodyning is that due to the high-bandwidth nature of an electrical

sawtooth wave, a large analog bandwidth is required from both the modulator and the control electronics.

To realize this, we utilize a segmented-electrode PM⁴⁵. This design increases the microwave index of the electrode, allowing us to achieve microwave-optical velocity matching with a smaller impedance penalty than achieved previously (see supplementary information section 1 for supporting data and simulations). In addition, this electrode design exhibits decreased Ohmic losses due to the breaking of the current path on the inner portion of the electrode^{45–47}. With this design, we realize high-bandwidth phase modulators with estimated 3 dB bandwidths of 55 GHz (>100 GHz) with respect to 2 GHz (5 GHz) response, which is a considerable enhancement over previously achieved results (35 GHz with respect to 3 GHz response)²⁵ (Fig. 4b). We estimate an on-chip optical loss of 0.7 dB for a 1 cm device (see methods).

Utilizing this modulator we perform a proof-of-principle serrodyne frequency shifting demonstration. We apply a sawtooth electrical waveform onto the phase modulator using a fast arbitrary waveform generator (AWG) and radio-frequency (RF) amplifier. The transmitted light is measured in the frequency domain by a scanning Fabry-Perot (FP) cavity. We observe frequency shifts of 1 GHz with high (>90%) efficiencies (Fig. 4c). To understand the limits of this serrodyning technique, we sweep the shift frequency and measure the efficiency (Fig. 4d). We find that there is an efficiency roll-off at higher frequencies attributed to the limited analog electrical bandwidth of 35 GHz amplifier used in our experiments. A model considering the finite bandwidth of the amplifier accurately reproduces our results, as shown in Fig. 4d (see supplementary information section 1 for model information). Despite this, we are still able to achieve shifts up to 15 GHz with shift efficiencies beyond 50%. Notably, this is sufficient to overcome the inhomogeneous distribution of various diamond QMs^{11,48}, and a significant improvement over previous demonstrations which were limited to ± 5 GHz^{43,44}. Going forward, we note that using state-of-the-art commercially available high-bandwidth electronics, shifts beyond the 15 GHz demonstrated in this work can be achieved using the same modulator (Fig. 4d, see supplementary information section 1 for details)^{49,50}. This demonstrates the utility of our PMs coupled with serrodyning technique to achieve ultra-large frequency

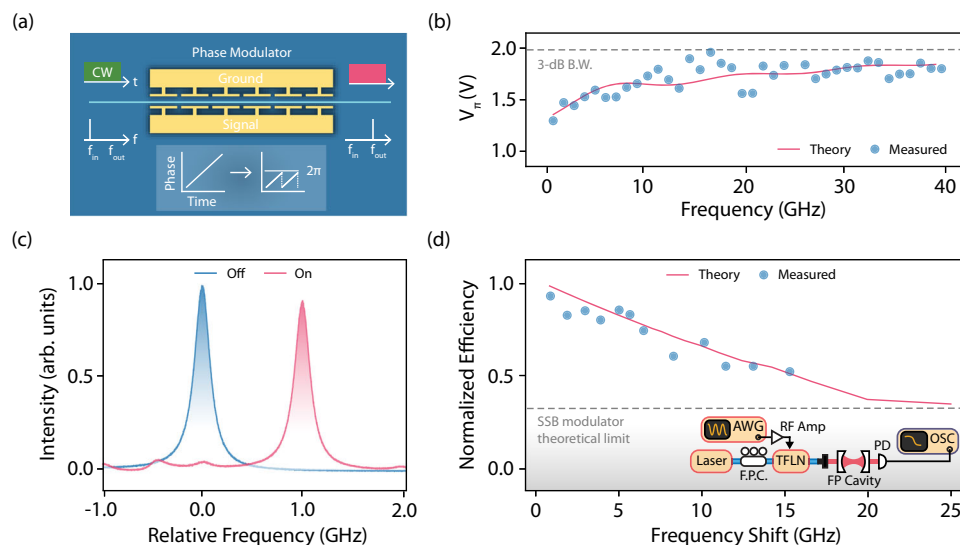


Fig. 4 | High-Bandwidth Phase Modulator for Frequency Shifting. **a** Schematic of phase modulator utilizing segmented electrodes to achieve high-bandwidth EO performance. An input optical signal is frequency shifted using EO serrodyning, where a linear increase in optical phase is approximated via a periodic sawtooth wave whose amplitude corresponds with a phase of 2π . **b** Half-wave voltage (V_{π}) as a function of frequency for a 1 cm phase modulator, showing a 3-dB EO bandwidth

exceeding 40 GHz (~100 GHz simulated). **c** Frequency spectrum of light transmitted through the phase modulator with the serrodyne electrical signal turned off (blue) or on (red), demonstrating a high-efficiency (>90%) 1 GHz frequency shift. **d** Serrodyne shift efficiency as a function of frequency shift, showing efficiencies greater than 50% for frequency shifts up to 15 GHz.

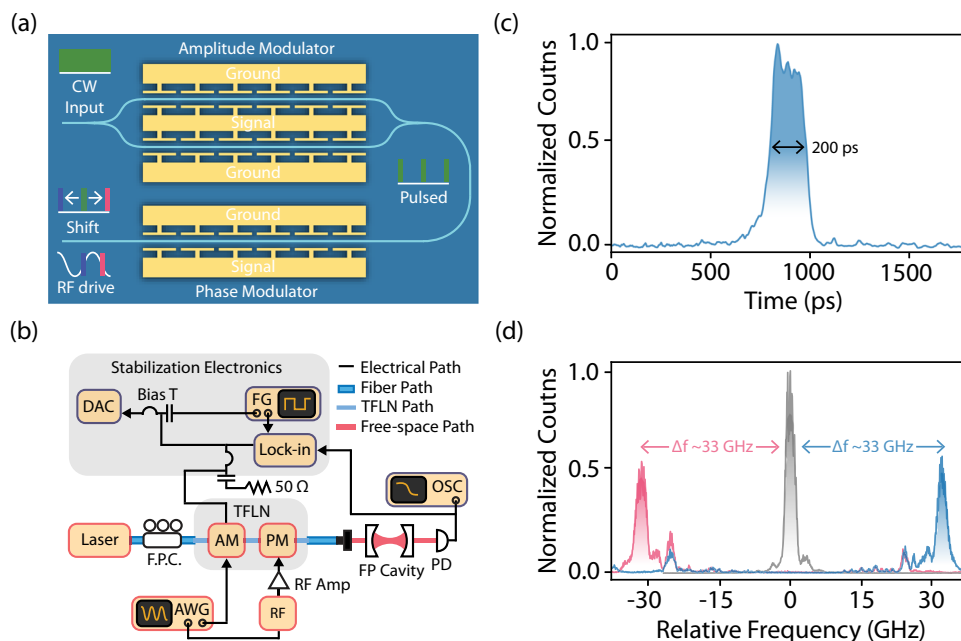


Fig. 5 | Laser control unit (LCU). **a** Schematic of LCU, that combines an AM to form optical pulses, and PM for frequency shifting via optical shearing effect of laser light. **b** Diagram of the experimental setup used to characterize LCU. **c** Temporal

profile of the generated pulse with pulse width down to 200 ps. **d** Frequency spectrum of generated and frequency-shifted optical pulses. A shift of ± 33 GHz is demonstrated.

shifts, with small added loss, for overcoming the inhomogeneous distribution of solid-state QMs.

To control QMs, CW and pulsed laser signals are needed. Inhomogeneous broadening of QMs, however, requires laser light of different wavelengths and pulse durations. One approach would be to utilize integrated photonic lasers with emission wavelengths tuned to particular QMs of interest^{31,52}. This approach does not scale well, as it would require an individual laser per quantum memory. QM optical control typically requires low laser linewidth for high-fidelity operations (kHz) and low optical power. As laser optical power and laser linewidth are inversely correlated^{53,54}, it is most efficient to have one integrated, higher power and low linewidth laser driving multiple QMs. This can be achieved using a laser control unit (LCU, Fig. 1) consisting of an AM followed by a PM (Fig. 5a) for each QM. This combination not only enables the amplitude and frequency shaping of input CW light to generate optical control pulses to interface with QMs but also shows the ability of our platform to support complex PICs containing multiple nested devices.

To illustrate the capabilities of the LCU, we implement a pulse shaping and shearing protocol to create a train of short pulses, and subsequently shift their central frequency. The AM is used to carve short pulses, which are then sent to a PM and temporally aligned with the linear rising/falling region of an applied sinusoidal tone (Fig. 5a). This introduces a frequency shift, and is commonly referred to as EO shearing^{55–57}. We have previously demonstrated state-of-the-art EO shearing with TFLN modulators, measuring maximum shifts of over 7 times the pulse linewidth²⁵. However, in that work, the pulse generation was done with a separate commercial AM. As the LCU contains both an AM and PM, we are able to perform amplitude and frequency shaping operations within the same PIC.

We utilize an electronic setup similar to our previous demonstration, with both the sinusoidal tone and the electrical pulses originating from a common AWG. The sinusoidal tone and RF pulses are applied to the PM and AM, respectively (Fig. 5b). We bias the amplitude modulator at the null point for pulse generation using a quasi-DC electro-optic bias whereby a feedback loop is applied to the low-frequency electrical bias of the modulator loop to

overcome the DC bias drift prevalent in TFLN modulators^{36,58}. As our modulators are optimized to minimize bias drift, we are able to compensate for the drift using off-the-shelf electronics and a simple software-based feedback loop. This demonstration thus highlights the ability of our devices to be biased purely electrically with minimal feedback, enabling their operation in cryogenic environments (see supplementary information section 2 for additional discussion).

Short (200 ps) optical pulses are generated by the AM directly driven by the AWG (Fig. 5c), which is faster than typically required for quantum optical control pulses. We then apply a 250 MHz sinusoidal tone to the PM and measure the resultant frequency spectrum via an FP cavity (Fig. 5d). We find that we can deterministically shift our optical pulses by ± 33 GHz. This corresponds to a drive amplitude of $40V_\pi$ and a shift of over 16 times the linewidth (see supplementary information section 1 for details). This large shift is sufficient to cover the inhomogeneous distribution of a variety of different emitters, providing a method for creating optical pulses to address different emitters, all while being seeded by a single laser. We observe some distortion is induced via shearing, as seen in the spectrum of the sheared transmission spectra. We hypothesize that this distortion is due to the inherent nonlinearity of the sinusoidal drive signal used in our experiment (see supplementary information section 1 for details on the model). We believe that LCU will be crucial to limit the complexity of optical control while scaling up the number of qubits per node. Through direct integration of the laser within the PIC, its scalability can be enhanced even further⁵². Beyond this, these findings demonstrate the ability to create complex, multi-element PICs with our platform.

Discussion

In this work, we have demonstrated the necessary ingredients to create PICs for multiplexing quantum network nodes, including state-of-the-art modulators, switches, and high-efficiency couplers. Using this platform we have shown proof of principle demonstrations of its utility, including frequency shifting a CW tone beyond 15 GHz with efficiencies above 50% and creating multi-element PICs to provide

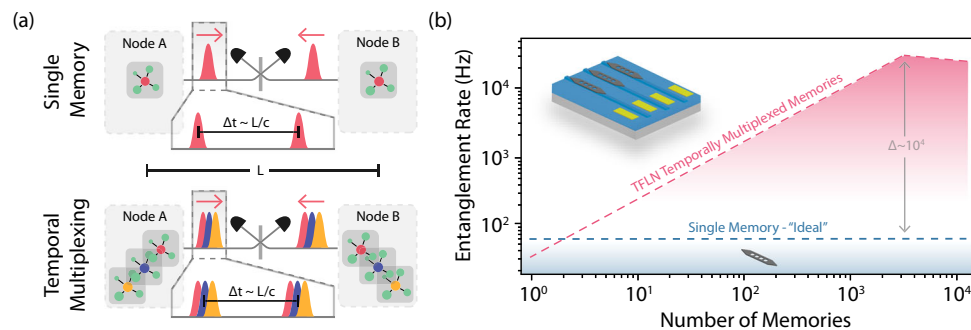


Fig. 6 | TFLN Enabled Temporal Multiplexing Advantage. **a** Diagram of remote entanglement generation scheme between two quantum nodes separated by a distance L (top) with a single memory or (bottom) using multiple memories interleaved via temporal multiplexing. **b** Computed entanglement rate between two quantum memories separated by $L = 20$ km utilizing temporal multiplexing as a

function of number of memories used. Losses of our platform are incorporated in this model. Due to the low-loss and scalability of our TFLN devices, a gain of over 100x in entanglement rate can be achieved via temporal multiplexing as compared to the single memory case.

amplitude and frequency control of optical pulses for simplifying optical control complexity at scale.

To contextualize the potential of this platform, we compute the benefits of temporal multiplexing using the TFLN-based architecture in Fig. 1 and our demonstrated device performance. We consider the model of two quantum nodes separated by a distance L , where each node probabilistically generates a flying photon entangled with the local spin memory and sent to a central station where a detection of one of the photons heralds entanglement (see supplementary information section 2 for details) (Fig. 6). For discussion purposes we focus on solid-state defects in diamond, and specifically the silicon-vacancy center in diamond, due to their excellent optical and spin properties and ability to be fabricated at scale^{11,13,59–61}. Owing to the wide transparency window of TFLN (>400 nm) we emphasize that this PIC platform is compatible with many other quantum memories, including quantum dots, trapped atoms, and rare-earth doped crystals, which also emit at visible wavelengths (see supplementary information section 2 for a discussion of compatible quantum memories). We consider two cases. The first is where only a single memory exists at each quantum node, and each node must wait the classical signaling time (L/c) between each entanglement attempt, limiting the repetition rate. The second case is where each quantum node has multiple memories which can be temporally interleaved via our TFLN PIC. This allows a significant increase in the repetition rate limited by the number of memories at each node and ultimately by the photon length, at the cost of additional losses from the TFLN PIC including coupling losses, frequency shifting losses, and device losses. In our calculations, we considered propagation losses of 0.3 dB/km typical of optical fibers at 1350 nm. We also included a 3 dB loss associated with frequency down-conversion of 737 nm photon to 1350 nm that is typical in state-of-the-art PPLN components^{8,62,63}. We compute the achievable entanglement rates across a 20 km channel for these two cases utilizing a silicon-vacancy center in diamond-based quantum memory. In the temporal multiplexing case we incorporate the estimated losses of the PIC including both individual device loss and off-chip coupling losses (see supplementary information section 2 for full model details). Despite the additional overhead of the TFLN PIC, we estimate the advantage of temporal multiplexing will lead to an enhanced entanglement rate with even a modest number of memories (<10) with an over 100x increase in rate achievable through saturation of the channel temporally (requiring ~ 2000 memories) (Fig. 6b). At larger channel lengths, we estimate that by using TFLN based temporal multiplexing we can maintain entanglement rates in excess of a kHz for lengths beyond 60 km. Although this is lower in absolute rate compared to the 20 km channel due to the exponential increase of loss with fiber length, it is

over three orders of magnitudes larger than that achieved with a single quantum memory (see SI). Through additional wavelength division multiplexing (WDM) using current telecom WDM technology, we estimate MHz entanglement rates can be achieved across the 20 km distance. This therefore demonstrates our platform achieves the necessary performance metrics and scalability to enable multiplexing and maximize quantum network performance.

Using this platform, future work will focus on increasing the complexity of visible TFLN PICs through increasing the number of elements and integrating with quantum memory systems to demonstrate the advantage of scalability. In addition, the future integration of thin film periodically-poled lithium niobate structures within the platform can decrease system complexity and enable higher efficiency visible to telecom conversion to achieve performance beyond that projected in Fig. 6^{64,65}. Furthermore, future work can investigate the integration of other materials into the platform such as III-V for on-chip classical and non-classical light sources and photodetectors^{52,66,67}, silicon-nitride for ultra low-loss waveguides⁶⁸, or superconducting circuits to further minimize power dissipation of the PIC and enable hybrid microwave-optical systems^{69–71}. Together these can enable novel functionalities for new quantum architectures. Moreover, due to the state-of-the-art performance of these devices, this platform can be applied to other quantum technology applications, such as control of atomic platforms, and even classical applications such as AR/VR, sensing, or communications operating in the visible region.

Methods

Device fabrication

All TFLN devices were realized on thin film wafers from NanoLN (X-cut, 300 nm LN/7 μ m SiO₂/500 μ m Si). Integrated photonic devices are fabricated by first patterning waveguide layers using electron-beam lithography (HSQ, Elionix ELS-F125), and etching ~ 180 nm using reactive ion etching (Ar⁺). This is then followed by re-deposition cleaning (RCA SC-1) and a high-temperature anneal (520 °C). For fabrication details please see ref. 25.

Modulator measurements

For low-frequency measurements, a variable frequency function generator produces a triangular waveform that is directed to the MZM electrodes using a 50 Ω ground-signal-ground probe (40A-GSG-100-F). A CW laser ($\lambda = 730$) is coupled to the modulator and out-coupled to an avalanche photodetector (APD410A). The detector output is monitored on an electronic oscilloscope, from which the V_{π} is extracted.

For high-frequency V_π measurements, a sinusoidal RF tone is applied at varying frequencies and the resulting optical spectrum is measured. The optical frequency spectrum of an MZM given an input CW optical carrier frequency of ω_0 , an applied RF tone at frequency ω_m and amplitude V_0 , and internal phase between the arms of ϕ is given by:

$$I(\omega_0 + k\omega_m) \propto \frac{1}{2} J_k^2(\pi V_0/V_\pi) [1 + (-1)^k \cos(\phi)] \quad (1)$$

where k is an integer of the harmonic of the drive frequency⁷².

The frequency spectrum is measured using a home-built Fabry-Perot cavity (linewidth = 200 MHz) and fit to (1).

For loss measurements, propagation loss was assumed to be the dominant loss, which was extracted via cutback measurements to be 0.7 dB/cm²⁵.

Serrodyne demonstration

Sawtooth electrical waveforms were generated using a fast arbitrary waveform generator (92 GSa, Keysight) and amplified via a high-bandwidth high-power amplifier. Pre-compensation is applied by the AWG to compensate for frequency-dependent loss-induced distortions from both the cables and the amplifier itself. The frequency spectrum of light transmitted through the modulator was measured via a scanning Fabry-Perot cavity. To compute the shift efficiency, the frequency spectrum of light transmitted through the modulator was measured with and without the applied sawtooth in quick succession to limit any setup drifts. The ratio of power in the shifted sideband to the initial unperturbed power was taken as the efficiency.

Shearing demonstration

To bias the amplitude modulator at the null point, a dither-based feedback was used. A small sinusoidal frequency at a low frequency (1 kHz) was combined with a DC offset via a bias tee and then applied to the amplitude modulator via a second bias tee. The transmitted light was then detected on a photodetector and the voltage output routed to a lock in amplifier to demodulate the dither signal and provide an error value. A software-based PID loop was then used to feedback the DC bias on this error value and ensure the amplitude modulator was locked to the null point.

With the amplitude modulator biased at the null point, short electrical pulses were applied to the amplitude modulator to generate the optical pulses while a sinusoidal tone was applied to the phase modulator. Both were generated by the same AWG (Tektronix 70000). For the shearing demonstration, an optical pulse length of 400 ps was used. Although shorter pulses could be generated, the total frequency shift with these pulses would be larger than the free-spectral range of the FP cavity (70 GHz) leading to aliasing artifacts.

We also note that the phase modulator was operated in lumped element configuration with no termination. This was possible due to the electrical narrowband nature of shearing.

Adiabatic coupler design

We simulate this coupler using an eigenmode expansion (EME) solver (Lumerical) to calculate the splitting ratio and the corresponding extinction ratio of the modulator as a function of length. We find that the coupler reaches the adiabatic condition at a length of 100 m. While there is still a variation of splitting ratio and extinction for longer lengths, the worst-case extinction ratio is still 15 dB, thus ensuring fabrication robustness. The simulated insertion loss is negligible (~0.01 dB).

Data availability

The data presented in this study is available from the corresponding authors upon request.

References

- Kimble, H.J. The quantum internet. *Nature* **453**. <https://doi.org/10.1038/nature07127> (2008).
- Wehner, S., Elkouss, D. & Hanson, R. Quantum internet: a vision for the road ahead. *Science* **362**. <https://doi.org/10.1126/science.aam9288> (2018).
- Covey, J.P., Weinfurter, H. & Bernien, H. Quantum networks with neutral atom processing nodes. *NPJ Quant. Inf.* **9**. <https://doi.org/10.1038/s41534-023-00759-9> (2023).
- Hensen, B. et al. Loophole-free Bell inequality violation using electron spins separated by 1.3 kilometres. *Nature* **526**. <https://doi.org/10.1038/nature15759> (2015).
- Hermans, S.L. et al. Qubit teleportation between non-neighbouring nodes in a quantum network. *Nature* **605**. <https://doi.org/10.1038/s41586-022-04697-y> (2022).
- van Leent, T. et al. Entangling single atoms over 33 km telecom fibre. *Nature* **607**. <https://doi.org/10.1038/s41586-022-04764-4> (2022).
- Delteil, A. et al. Generation of heralded entanglement between distant hole spins. *Nat. Phys.* **12**. <https://doi.org/10.1038/nphys3605> (2016).
- Knaut, C. M. et al. Entanglement of nanophotonic quantum memory nodes in a telecommunication network. *Nature* **629**, 573 (2024).
- Duan, L.M., Lukin, M.D., Cirac, J.I. & Zoller, P. Long-distance quantum communication with atomic ensembles and linear optics. *Nature* **414**. <https://doi.org/10.1038/35106500> (2001).
- Bennett, C.H. et al. Purification of noisy entanglement and faithful teleportation via noisy channels. *Phys. Rev. Lett.* **76**. <https://doi.org/10.1103/PhysRevLett.76.722> (1996).
- Evans, R. E., Sipahigil, A., Sukachev, D. D., Zibrov, A. S. & Lukin, M. D. Narrow-linewidth homogeneous optical emitters in diamond nanostructures via silicon ion implantation. *Phys. Rev. Appl.* **5**, 044010 (2016).
- Ruf, M., Wan, N. H., Choi, H., Englund, D. & Hanson, R. Quantum networks based on color centers in diamond. *J. Appl. Phys.* **130**. <https://doi.org/10.1063/5.0056534> (2021).
- Lukin, D.M., Guidry, M.A. & Vučković, J. Integrated quantum photonics with silicon carbide: challenges and prospects. *PRX Quantum* **1**. <https://doi.org/10.1103/PRXQuantum.1.020102> (2020).
- Kindem, J. M. et al. Control and single-shot readout of an ion embedded in a nanophotonic cavity. *Nature* **580**. <https://doi.org/10.1038/s41586-020-2160-9> (2020).
- Krutyanskiy, V. et al. Entanglement of trapped-ion qubits separated by 230 meters. *Phys. Rev. Lett.* **130**. <https://doi.org/10.1103/PhysRevLett.130.050803> (2023).
- Sund, P.I. et al. High-speed thin-film lithium niobate quantum processor driven by a solid-state quantum emitter. *Sci. Adv.* **9**. <https://doi.org/10.1126/sciadv.adg7268> (2023).
- Zhai, L. et al. Low-noise GaAs quantum dots for quantum photonics. *Nat. Commun.* **11**, 4745 (2020).
- Zeng, B. et al. Cryogenic packaging of nanophotonic devices with a low coupling loss <1 db. *Appl. Phys. Lett.* **123**, 161106 (2023).
- Mohanty, A. et al. Reconfigurable nanophotonic silicon probes for sub-millisecond deep-brain optical stimulation. *Nat. Biomed. Eng.* **4**. <https://doi.org/10.1038/s41551-020-0516-y> (2020).
- Sacher, W. D. et al. Visible-light silicon nitride waveguide devices and implantable neurophotonic probes on thinned 200 mm silicon wafers. *Opt. Express* **27**, 37400 (2019).
- Dong, M. et al. High-speed programmable photonic circuits in a cryogenically compatible, visible-near-infrared 200 mm CMOS architecture. *Nat. Photonics* **16**, 59–65 (2022).
- Zhang, C. et al. Integrated photonics beyond communications. *Appl. Phys. Lett.* **123**, 230501 (2023).
- Zhu, D. et al. Integrated photonics on thin-film lithium niobate. *Adv. Opt. Photonics* **13**. <https://doi.org/10.1364/aop.411024> (2021).

24. Desiatov, B., Shams-Ansari, A., Zhang, M., Wang, C. & Lončar, M. Ultra-low-loss integrated visible photonics using thin-film lithium niobate. *Optica* **6**. <https://doi.org/10.1364/optica.6.000380> (2019).
25. Renaud, D. et al. Sub-1 volt and high-bandwidth visible to near-infrared electro-optic modulators. *Nat. Commun.* **14**. <https://doi.org/10.1038/s41467-023-36870-w> (2023).
26. Christen, I. et al. An integrated photonic engine for programmable atomic control. <https://arxiv.org/abs/2208.06732> (2024).
27. Valdez, F., Mere, V. & Mookherjee, S. 100 GHz bandwidth, 1 volt integrated electro-optic mach-zehnder modulator at near-ir wavelengths. *Optica* **10**. <https://doi.org/10.1364/optica.484549> (2023).
28. Burek, M. J. et al. Fiber-coupled diamond quantum nanophotonic interface. *Phys. Rev. Appl.* **8**. <https://doi.org/10.1103/PhysRevApplied.8.024026> (2017).
29. Khan, S. et al. Low-loss, high-bandwidth fiber-to-chip coupling using capped adiabatic tapered fibers. *APL Photonics* **5**. <https://doi.org/10.1063/1.5145105> (2020).
30. Tiecke, T. G. et al. Efficient fiber-optical interface for nanophotonic devices. *Optica* **2**. <https://doi.org/10.1364/optica.2.000070> (2015).
31. He, L. et al. Low-loss fiber-to-chip interface for lithium niobate photonic integrated circuits. *Opt. Lett.* **44**. <https://doi.org/10.1364/ol.44.002314> (2019).
32. Lomonte, E., Lenzini, F. & Pernice, W.H.P. Efficient self-imaging grating couplers on a lithium-niobate-on-insulator platform at near-visible and telecom wavelengths. *Opt. Express* **29**. <https://doi.org/10.1364/oe.428138> (2021).
33. Hu, C. et al. High-efficient coupler for thin-film lithium niobate waveguide devices. *Opt. Express* **29**. <https://doi.org/10.1364/oe.416492> (2021).
34. Cao, L., Elshaari, A., Aboketaf, A. & Preble, S. Adiabatic couplers in soi waveguides. CLEO: Science and Innovations, CLEO-SI 2010. <https://doi.org/10.1364/cleo.2010.cthaa2> (2010).
35. Yun, H. et al. 2×2 broadband adiabatic 3-db couplers on SOI strip waveguides for TE and TM modes. CLEO: Science and Innovations. (CLEO-SI 2015, 2015).
36. Holzgrafe, J. et al. Relaxation of the electro-optic response in thin-film lithium niobate modulators. *Opt. Express* **32**, 3619–3631 (2024).
37. Nguyen, C. T. et al. An integrated nanophotonic quantum register based on silicon-vacancy spins in diamond. *Phys. Rev. B* **100**, 165428 (2019).
38. Bradac, C., Gao, W., Forneris, J., Trusheim, M. E. & Aharonovich, I. Quantum nanophotonics with group iv defects in diamond. *Nat. Commun.* **10**, 5625 (2019).
39. Holland, C.M., Lu, Y. & Cheuk, L.W. Synthesizing optical spectra using computer-generated holography techniques. *New J. Phys.* **23**. <https://doi.org/10.1088/1367-2630/abe973> (2021).
40. Johnson, D. M. S., Hogan, J. M., w. Chiow, S. & Kasevich, M. A. Broadband optical serrodyne frequency shifting. *Opt. Lett.* **35**. <https://doi.org/10.1364/ol.35.000745> (2010).
41. Houtz, R., Chan, C. & Müller, H. Wideband, efficient optical serrodyne frequency shifting with a phase modulator and a nonlinear transmission line. *Opt. Express* **17**. <https://doi.org/10.1364/oe.17.019235> (2009).
42. Poberezhskiy, I. Y., Bortnik, B., Chou, J., Jalali, B. & Fetterman, H. R. Serrodyne frequency translation of continuous optical signals using ultrawide-band electrical sawtooth waveforms. *IEEE J. Quantum Electron.* **41**. <https://doi.org/10.1109/JQE.2005.858467> (2005).
43. Sinclair, N. et al. Spectral multiplexing for scalable quantum photonics using an atomic frequency comb quantum memory and feed-forward control. *Phys. Rev. Lett.* **113**. <https://doi.org/10.1103/PhysRevLett.113.053603> (2014).
44. Saglamyurek, E. et al. An integrated processor for photonic quantum states using a broadband light-matter interface. *New J. Phys.* **16**. <https://doi.org/10.1088/1367-2630/16/6/065019> (2014).
45. Kharel, P., Reimer, C., Luke, K., He, L. & Zhang, M. Breaking voltage-bandwidth limits in integrated lithium niobate modulators using micro-structured electrodes. *Optica* **8**. <https://doi.org/10.1364/optica.416155> (2021).
46. Ding, R. et al. High-speed silicon modulator with slow-wave electrodes and fully independent differential drive. *J. Lightwave Technol.* **32**. <https://doi.org/10.1109/JLT.2014.2323954> (2014).
47. Shin, J., Sakamoto, S. R. & Dagli, N. Conductor loss of capacitively loaded slow wave electrodes for high-speed photonic devices. *J. Lightwave Technol.* **29**. <https://doi.org/10.1109/JLT.2010.2091624> (2011).
48. Machielse, B. et al. Quantum interference of electromechanically stabilized emitters in nanophotonic devices. *Phys. Rev. X* **9**, 031022 (2019).
49. Chen, X. et al. All-electronic 100-ghz bandwidth digital-to-analog converter generating pam signals up to 190 gbaud. *J. Lightwave Technol.* **35**. <https://doi.org/10.1109/JLT.2016.2614126> (2017).
50. Wakita, H., Jyo, T., Nagatani, M. & Takahashi, H. 108-ghz-bandwidth compact inp-hbt baseband amplifier module with integrated dc-block functions. *IEEE Microwave and Wireless Technol. Lett.* **33**. <https://doi.org/10.1109/LMWT.2023.3243233> (2023).
51. Tran, M. A., Huang, D. & Bowers, J. E. Tutorial on narrow linewidth tunable semiconductor lasers using si/iii-v heterogeneous integration. *APL Photonics* **4**, 111101 (2019).
52. Shams-Ansari, A. et al. Electrically pumped laser transmitter integrated on thin-film lithium niobate. *Optica* **9**, 408–411 (2022).
53. Henry, C. H. Theory of the linewidth of semiconductor lasers. *IEEE J. Quantum Electron.* **18**. <https://doi.org/10.1109/JQE.1982.1071522> (1982).
54. Coldren, L. A. L. A. Diode lasers and photonic integrated circuits 2nd ed. edn (Wiley, 2012).
55. Johnson, L.M. & Cox, C.H. Serrodyne optical frequency translation with high sideband suppression. *J. Lightwave Technol.* **6**. <https://doi.org/10.1109/50.3974> (1988).
56. Wright, L. J., Karpinski, M., Söller, C. & Smith, B. J. Spectral shearing of quantum light pulses by electro-optic phase modulation. *Phys. Rev. Lett.* **118**, 023601 (2017).
57. Zhu, D. et al. Spectral control of nonclassical light pulses using an integrated thin-film lithium niobate modulator. *Light Sci. Appl.* **11**. <https://doi.org/10.1038/s41377-022-01029-7> (2022).
58. Sosunov, A., Ponomarev, R., Zhuravlev, A., Mushinsky, S. & Kuneva, M. Reduction in dc-drift in linbo3-based electro-optical modulator. *Photonics* **8**. <https://doi.org/10.3390/photonics8120571> (2021).
59. Tchernij, S. D. et al. Single-photon-emitting optical centers in diamond fabricated upon sn implantation. *ACS Photonics* **4**. <https://doi.org/10.1021/acsphotonics.7b00904> (2017).
60. Doherty, M.W. et al. The nitrogen-vacancy colour centre in diamond. *Phys. Reports* **528**. <https://doi.org/10.1016/j.physrep.2013.02.001> (2013).
61. Bhaskar, M.K. et al. Experimental demonstration of memory-enhanced quantum communication. *Nature* **580**. <https://doi.org/10.1038/s41586-020-2103-5> (2020).
62. Leent, T.V. et al. Long-distance distribution of atom-photon entanglement at telecom wavelength. *Phys. Rev. Lett.* **124**. <https://doi.org/10.1103/PhysRevLett.124.010510> (2020).
63. Bersin, E. et al. Telecom networking with a diamond quantum memory. *PRX Quantum* **5**. <https://doi.org/10.1103/PRXQuantum.5.010303> (2024).
64. Xin, C. J. et al. Spectrally separable photon-pair generation in dispersion engineered thin-film lithium niobate. *Opt. Lett.* **47**. <https://doi.org/10.1364/ol.456873> (2022).
65. Xin, C. J. et al. Wavelength-accurate and wafer-scale process for nonlinear frequency mixers in thin-film lithium niobate. <https://arxiv.org/abs/2404.12381> (2024).

66. Snigirev, V. et al. Ultrafast tunable lasers using lithium niobate integrated photonics. *Nature* **615**. <https://doi.org/10.1038/s41586-023-05724-2> (2023).
67. Guo, X. et al. High-performance modified uni-traveling carrier photodiode integrated on a thin-film lithium niobate platform. *Photonics Res.* **10**. <https://doi.org/10.1364/prj.455969> (2022).
68. Bose, D. et al. Anneal-free ultra-low loss silicon nitride integrated photonics. *Light Sci. Appl.* **13**, 156 (2024).
69. Warner, H. K. et al. Coherent control of a superconducting qubit using light. *Nat. Commun.* **14**, 3784 (2023).
70. Xu, Y. et al. Bidirectional interconversion of microwave and light with thin-film lithium niobate. *Nat. Commun.* **12**. <https://doi.org/10.1038/s41467-021-24809-y> (2021).
71. Colangelo, M. et al. Molybdenum silicide superconducting nanowire single-photon detectors on lithium niobate waveguides. *ACS Photonics* **11**, 356–361 (2024).
72. Shi, Y., Yan, L. & Willner, A. E. High-speed electrooptic modulator characterization using optical spectrum analysis. *J. Lightwave Technol.* **21**. <https://doi.org/10.1109/JLT.2003.818162> (2003).

Acknowledgements

This work was supported in part by AFOSR FA9550-20-1-0105 (M.L., D.R.), AFOSR FA9550-19-1-0376 (M.L., A.S.A.), ARO MURI W911NF1810432 (D.R., D.B., M.L.), NSF EEC-1941583 (M.L., D.A., C.X.), NSF OMA-2137723 (M.L., C.X.), OMA-2138068 (M.L., M. Y.), AWS Center for Quantum Networking's research alliance with the Harvard Quantum Initiative (M.L., D.A., D.R., C.X.), Ford Foundation Fellowship, (D.R.), and NSF GRFP No. DGE1745303 (D.R., D.A.). Device fabrication was performed at the Center for Nanoscale Systems (CNS), a member of the National Nanotechnology Coordinated Infrastructure Network (NNCI), which is supported by the National Science Foundation under NSF Grant No. 1541959.

Author contributions

D.A., D.B., and D.R. designed devices. D.R., C.D., and C.X. fabricated devices. D.A., A.B., and B.Z. designed and performed the measurements. D.A. and D.R. analyzed the data. D.R., D.A., A.B., and A.S. wrote the manuscript with extensive input from the other authors. A.S., B.M., and M.L. supervised the project. These authors contributed equally: D.A. and D.R.

Competing interests

D.R. and M.L. are involved in developing lithium niobate technologies at HyperLight Corporation. The remaining authors declare no competing interests.

Additional information

Supplementary information The online version contains supplementary material available at <https://doi.org/10.1038/s41467-024-54541-2>.

Correspondence and requests for materials should be addressed to Daniel Assumpcao, Dylan Renaud or Marko Loncar.

Peer review information *Nature Communications* thanks Ali Elshaari and Sridhar Majety for their contribution to the peer review of this work. A peer review file is available.

Reprints and permissions information is available at <http://www.nature.com/reprints>

Publisher's note Springer Nature remains neutral with regard to jurisdictional claims in published maps and institutional affiliations.

Open Access This article is licensed under a Creative Commons Attribution-NonCommercial-NoDerivatives 4.0 International License, which permits any non-commercial use, sharing, distribution and reproduction in any medium or format, as long as you give appropriate credit to the original author(s) and the source, provide a link to the Creative Commons licence, and indicate if you modified the licensed material. You do not have permission under this licence to share adapted material derived from this article or parts of it. The images or other third party material in this article are included in the article's Creative Commons licence, unless indicated otherwise in a credit line to the material. If material is not included in the article's Creative Commons licence and your intended use is not permitted by statutory regulation or exceeds the permitted use, you will need to obtain permission directly from the copyright holder. To view a copy of this licence, visit <http://creativecommons.org/licenses/by-nc-nd/4.0/>.

© The Author(s) 2024